WILEY | Hindawi

Research Article

A Coupled Inductor-Based Bidirectional DC-DC Converter with Step-Up Step-Down Operation for Electric Vehicle Applications

Muhammad Zeeshan Malik [ID],[1] **Shiqing Zhang,[1] Yuanyuan Hong,[1]
Ayham Riyad A'Yesh Alwahkyan,[2] Amjad Ali** [ID],[3] **and Ajmal Farooq[4]**

[1]*School of Electronics and Information Engineering, Taizhou University, Taizhou, Zhejiang 318000, China*
[2]*College of Aeronautical Engineering, Taizhou University, Taizhou, Zhejiang 318000, China*
[3]*Interdisciplinary Research Center for Renewable Energy and Power Systems (IRC-REPS),*
 King Fahd University of Petroleum and Minerals, Dhahran 31261, Saudi Arabia
[4]*Department of Electrical Engineering, University of Engineering & Technology Mardan, Mardan, Pakistan*

Correspondence should be addressed to Muhammad Zeeshan Malik; malik4one@yahoo.com

A coupled-inductor-based high step-up high step-down DC-DC converter with bidirectional capability suitable for electric vehicle (EV) applications is proposed in this paper. The voltage gain in both step-up and step-down operations is increased by a two-winding coupled inductor. The current ripple in the low-voltage port is low making it suitable for renewable energy sources. In addition, the low number of components causes the efficiency of the proposed converter to be competitive with similar topologies in the literature. Due to the use of only three bidirectional switches with low voltage stress, the cost and volume of the converter are reduced. To demonstrate the performance of the proposed bidirectional converter, an analysis of the operation modes in the steady state is presented. Also, a comparison between the suggested converter and other similar converters in the literature is provided. The results of these comparisons show that the proposed converter has a lower number of components and higher efficiency than the others. In addition, lower voltage stress and noticeable voltage gain in comparison with others are further results of these comparisons. Eventually, the experimental results in step-up and step-down operations are presented. In step-up operation, the experimental prototype is tested under $fs = 50\,\text{kHz}$, $V_{\text{Low}} = 20\,\text{V}$, $V_{\text{High}} = 110\,\text{V}$, rated power = 120 W, with 94.60% efficiency. Furthermore, V_{High} is considered 100 V with $V_{\text{Low}} = 33\,\text{V}$ and 94.43% efficiency at 50 W rated power in step-down mode operation.

1. Introduction

In recent years, electric vehicles (EVs) utilization has risen because of the widespread evolution of environmental disintegration and circumstances such as economic crises and lack of fossil fuels [1, 2]. Due to using hybrid energy systems (HES) in EVs, the bidirectional power flow must be insured [3, 4]. Among the renewable sources, photovoltaic (PV) energy is stunning for generating electricity due to its pollution-free, scalable flexibility, and low maintenance [5, 6]. However, because of the dependence of its power on the level of sunlight, ambient temperature, and unexpected

shading, a PV-based system must be augmented with other alternative energy sources to ensure a reliable power supply [7, 8]. To overcome these challenges, bidirectional DC-DC converters have been developed in which the power can transfer in both directions between the input and output ports [9, 10].

Considerable types of research on bidirectional DC-DC converters have been presented in various articles. In [11], a bidirectional nonisolated DC-DC converter consisting of power storage units is presented for HESs in EVs. This converter has acceptable performance in both charging and discharging modes. As a result, the output voltage of the

converter might be greater than or less than the input voltage. For distributed energy storage systems, the authors of [12] introduce a bidirectional high-voltage gain DC-DC converter based on switched capacitors and coupled inductors. However, due to the enormous number of power switches employed, it is not a high-efficiency and cost-effective topology. The topology presented in [13] features a buck-boost function and can be utilized in EVs. The voltage gain of this topology, however, is lower than those of other comparable converters. In [14], a three-port bidirectional topology for HES is presented. This converter offers a soft-switching feature, which results in reduced losses and excellent efficiency. This topology, however, has a significant input current ripple, so the CCM is not achieved in all modes. A topology for HES is presented in [15]. This converter has step-down, step-up, and buck-boost operations. Nevertheless, it is restricted by high peak voltage on the semiconductor. The authors in [16] give a bidirectional multiport topology to regulate bidirectional power in hybrid battery systems. Nonetheless, a huge number of semiconductors are used. A DC-DC topology for EVs with HES is given in [17–19]. The enormous number of components is the main downside of these structures. Isolated bidirectional topologies are presented in [20, 21]. A costly transformer is included in the structure of these two converters. Furthermore, converters [22, 23] have a large voltage gain as well as a low peak voltage of the switches and diodes. These converters can even be interconnected to diverse power inputs. However, these structures suffer from a lack of bidirectional power flow. As a result, they are unsuitable for HESs. In [24], a switched capacitor-based topology is recommended for EV application. The low number of components, low voltage stress across power switches, and simple structure are its main advantages. A nonisolated multiport DC-DC converter consisting of a battery port is presented in [25]. The high number of semiconductors, lack of bidirectional power flow, and its inability to simultaneously transfer inputs power to the output ports are the major weaknesses of this converter. A transformer-less bidirectional multiport DC-DC converter is given in [26]. Continuous charging/discharging current of the battery, low normalized peak voltage stress (NPVS) on semiconductors, and step-up capability are advantages of this converter. However, the input and output ports do not share a common ground. The authors introduce a dual-input DC-DC converter with bidirectional power flow [27]. Step-up capability, the low voltage stress on semiconductors, and the smaller number of passive elements are advantages of the converter. The use of a high number of switches is the main drawback of this topology. An interleaved soft-switched boost converter without any auxiliary switch is given in [28]. Smaller current stress of the devices, low conduction and switching losses, and its simple control system are the main benefits of this converter. The authors in [29] have designed a series LC-basedsingle-stage boost converter and expanded its voltage gain by a multistage boost converter using the switched capacitor method. This converter has only one auxiliary switch and works using the minimum number of components required to create a very high voltage gain DC-DC converter. A simple and

systematic method to synthesize a robust adaptive fuzzy fractional-order nonsingular terminal sliding mode controller to enhance the output voltage tracking control performance of the DC-DC step-down converters is presented in [30]. Improved flexibility acquired by fractional-order computation, enhancing robustness to disruptions and parameter variations provided by the conventional sliding mode controllers as well as finite time convergence properties of the output voltage error to the balance point during the output load variations, simultaneously is the main advantage of this idea. A high step-up DC-DC converter ideal for photovoltaic applications is given in [31]. Reduced current ripple, low voltage stress across the main and auxiliary switches, and soft-switching conditions of all switches and diodes are the major advantages of this topology. In Reference [32], an extendable high step-up topology is presented for the low input voltage applications, that is, fuel cell (FC) source. In the mentioned converter, the input current ripple is zero. However, an inductor has been added at the input, which does not increase the voltage gain and only reduces the input current ripple. Thus, the cost of the converter will be high.

In this paper, a new bidirectional high step-up, step-down DC-DC converter based on the coupled inductor technique is proposed for EV applications. A two-winding coupled inductor increases the voltage gain in both step-up and step-down operations. The current ripple in the low voltage port is low makes the proposed converter suitable for renewable energy sources. The lower number of components causes the power efficiency to be high. Also, due to the existence of only three bidirectional power switches with low voltage stress, the cost and volume of the converter are reduced.

The rest of the paper is organized as follows: Section 2 is devoted to the proposed topology explanation. Analysis of the operation principle is presented in Section 3. A steady-state analysis of the converter is done in Section 4. Design considerations and power loss analysis are investigated in Sections 5 and 6, respectively. A comparison with other solutions in the literature is accomplished in Section 7. The experimental results of a prototype-based converter are presented in Section 8, and the paper ends with a conclusion in Section 9.

2. Proposed Converter Description

The topology of the proposed converter is shown in Figure 1. As can be seen in this figure, the suggested converter has three bidirectional power switches (Q_1, Q_2, and Q_3), three capacitors (C_1, C_2, and C_3), and two magnetic cores, which one core is used for inductor L_1 and another one is used for the coupled inductor. The coupled inductor is modeled as an ideal transformer with the number of turns (n_1 and n_2), leakage, and magnetizing inductances (L_k and L_m). Also, the turns ratio of the coupled inductor is defined as $N = n_1/n_2$. V_{Low} is the voltage of the port with a lower voltage level, and V_{High} presents the voltage of the port with a higher voltage. This converter can operate in both step-up and step-down modes. In the next section, these operation modes are analyzed.
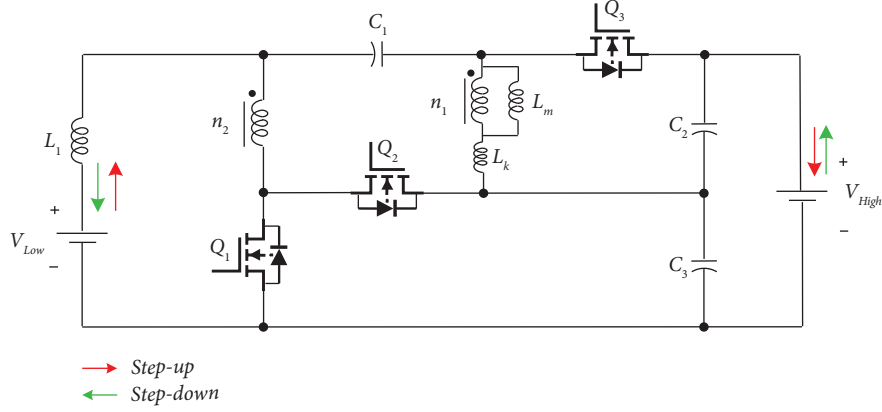
FIGURE 1: The power circuit of the suggested converter.

3. Analysis of the Operation Principle

The key waveforms of the proposed converter in step-up and step-down operation modes are shown in Figures 2(a) and 2(b), respectively. As can be seen from Figure 2, when switch Q_1 is turned on, switches Q_2 and Q_3 are turned off, and vice versa. In other words, switch Q_1 is switched in complementary with switches Q_2 and Q_3. If D_1, D_2, and D_3 are considered the duty cycle of Q_1, Q_2, and Q_3, respectively, the following equation is used in both operation modes according to Figure 2:

$$\begin{cases} D_1 T_s = (1 - D_2)T_s = (1 - D_3)T_s, \\ (1 - D_1)T_s = D_2 T_s = D_3 T_s. \end{cases} \tag{1}$$

3.1. Step-Up Operation Mode. This operation mode has two switching states. In both states, the power is transferred from V_{Low} to V_{High} which is discussed in detail as follows:

State 1: At the start of state 1, Q_1 is turned on while Q_2 and Q_3 are turned off. Therefore, the voltage across L_1 is positive, and its current is increased. However, the voltage across the primary side of the coupled inductor is equal to the voltage difference between C_1 and C_3, and it is negative. The load R_o is supplied by C_2 current. The current path of this switching state is shown in Figure 3(a).

$$V_{L1} = V_{\text{Low}} - NV_{Lm}, \tag{2}$$

$$V_{Lm}(1 - N) = V_{C1} - V_{C3}, \tag{3}$$

$$V_{\text{High}} = V_{C2} + V_{C3}, \tag{4}$$

$$i_{\text{Low}} = i_{Q1} + i_{C1}, \tag{5}$$

$$i_{C2} = -i_{\text{High}}, \tag{6}$$

$$i_{C3} = i_{Lk} - i_{\text{High}}. \tag{7}$$

State 2: This switching state starts when Q_1 is turned off, and two other switches are turned on. The voltage across L_1 obtained by (9) is negative, and so, its current is decreased. Vice versa, the voltage across the primary side of the coupled inductor is positive

resulting in increasing its leakage and magnetizing currents. C_1 is charged by the energy stored in the secondary winding of the coupled inductor. Also, the energy stored in L_k and L_m is transferred to C_2, C_3, and R_o. The equivalent circuit in this state is shown in Figure 3(b) resulting in the following equations:

$$V_{Lm} = V_{C2}, \tag{8}$$

$$V_{L1} = V_{\text{Low}} - V_{C3} - NV_{C2}, \tag{9}$$

$$V_{C1} = V_{Lm}(1 - N), \tag{10}$$

$$i_{Q3} = i_{\text{High}} + i_{C2}, \tag{11}$$

$$i_{C3} = i_{\text{Low}} - i_{\text{High}}, \tag{12}$$

$$i_{C1} = -(i_{Q3} + i_{Lk}), \tag{13}$$

$$i_{n2} = i_{Q2}. \tag{14}$$

3.2. Step-Down Operation Mode. The step-down mode also includes two switching states. In both states, the power is transferred from high voltage port VHigh to low voltage port VLow. It should be noticed that the output load R_o is linked to the port with a lower voltage level.

State 1: At the beginning of step-down mode, Q_2 and Q_3 are turned on while Q_1 is turned off. The voltage across L_1 calculated by (15) is positive. Thus, its current is increased. The energy of V_{High} is transferred to C_2, the primary side of the coupled inductor, and R_o through Q_2 and Q_3. On the other hand, C_1 and C_3 are discharged. The current path of state 1 in this mode is illustrated in Figure 4(a), and the equations are obtained as follows:

$$V_{L1} = V_{C3} + NV_{C2} - V_{\text{Low}}, \tag{15}$$

$$i_{\text{High}} = i_{Q3} + i_{C2} = i_{Lk} + i_{C1} + i_{C2}, \tag{16}$$

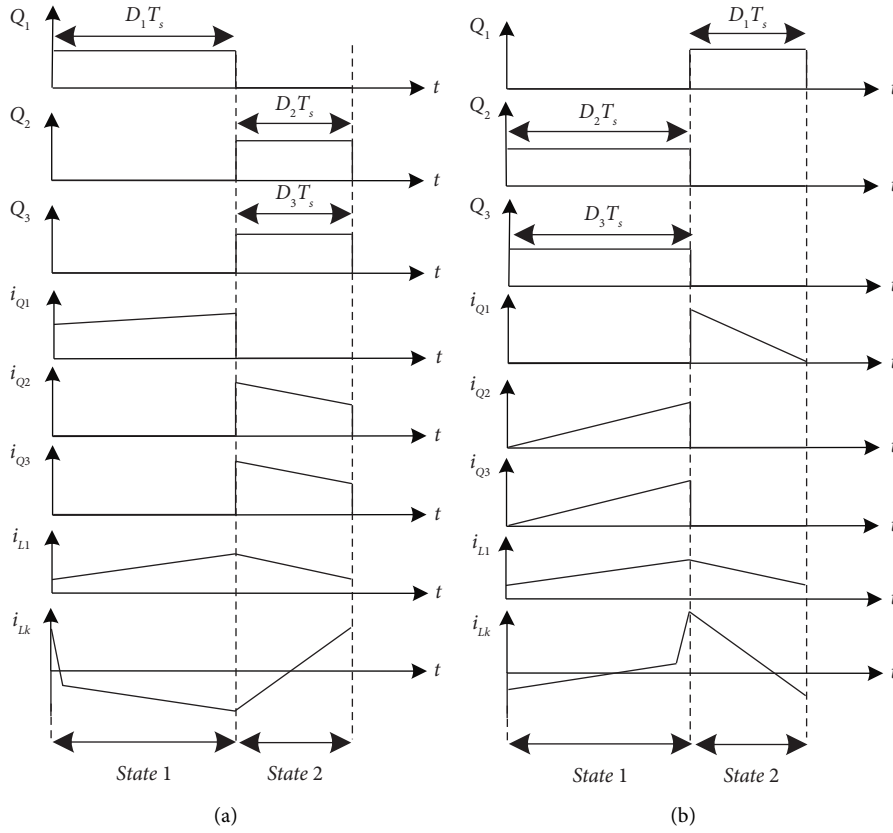$$i_{L1} = i_{Q2} + i_{C1} = i_{\text{Low}} + i_{CL}. \tag{17}$$

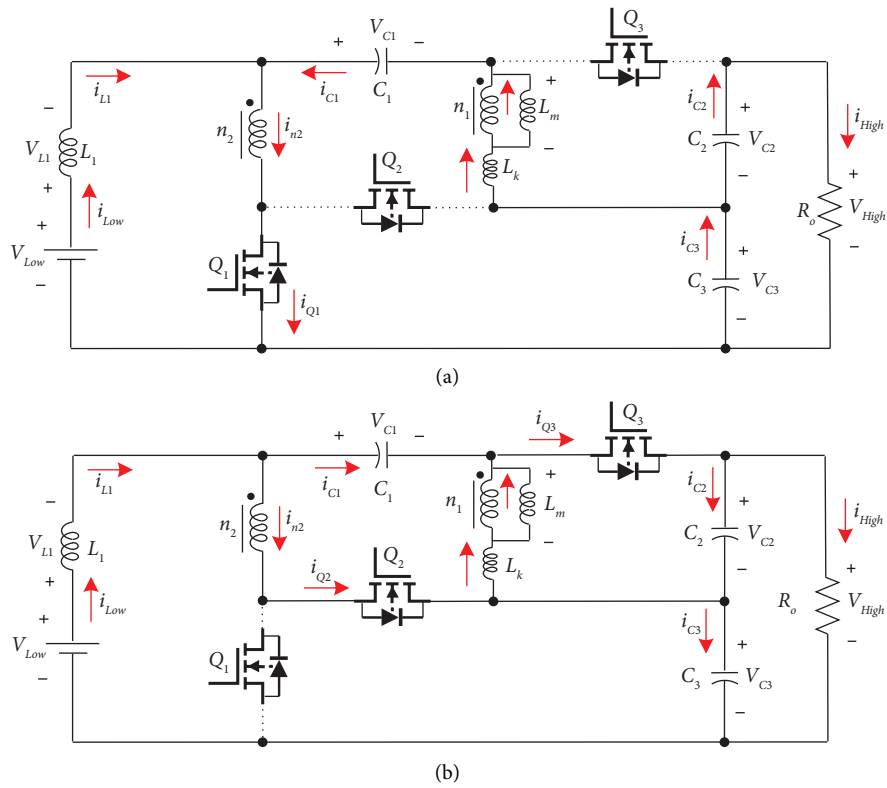FIGURE 2: The main waveforms: (a) step-up mode and (b) step-down mode.

FIGURE 3: The equivalent circuits in step-up mode: (a) state 1 and (b) state 2.

State 2: This switching state starts when Q_2 and Q_3 are turned off, and Q_1 is turned on. Same as state 2 at step-up mode, the voltage across L_1 is negative. Therefore, its current is decreased, and vice versa, the voltage across the primary side of the coupled inductor is positive, and its leakage and magnetizing currents are increased. During this switching state, C_1 and C_3 are charged by the energy stored in the coupled inductor. The equivalent circuit of state 2 in step-down mode is depicted in Figure 4(b).

$$V_{L1} = N V_{Lm} - V_{\text{Low}}. \tag{18}$$

4. Steady-State Analysis

In this section, the voltage gain of the proposed converter in step-up and step-down operation modes, peak voltage across power switches, and the current of used elements is analyzed.

4.1. Voltage Calculation. Using the volt-second balance law on inductor L_m, the following equation is achieved:

$$\langle V_{Lm} \rangle_{T_s} = 0 \longrightarrow D_1\left(\frac{V_{C1} - V_{C3}}{1 - N}\right) + (1 - D_1)\frac{V_{C1}}{1 - N} = 0. \tag{19}$$

With the simplification of (19), the voltage of capacitor C_1 can be written versus V_{C3}:

$$V_{C1} = D_1 V_{C3}. \tag{20}$$

Also, using (8) and (10), the voltage of capacitor C_1 can be written versus V_{C2}:

$$V_{C1} = (1 - N) V_{C2}. \tag{21}$$

Using the volt-second balance law on inductor L_1, equation (22) can be expressed as follows:

$$\langle V_{L1} \rangle_{T_s} = 0 \longrightarrow D_1 V_{\text{Low}} + D_1\left(\frac{N(1 - D_1)}{1 - N} V_{C3}\right) + (1 - D_1) V_{\text{Low}} = 0. \tag{22}$$

Simplifying (22) causes the voltage of capacitor C_3 to be calculated versus V_{Low} and power switches duty cycles:

$$V_{C3} = \frac{V_{\text{Low}}}{1 - D_1} = \frac{V_{\text{Low}}}{D_2}. \tag{23}$$

Therefore, V_{C1} and V_{C2} can be written as follows:

$$V_{C1} = \frac{D_1 V_{\text{Low}}}{1 - D_1}, \tag{24}$$

$$V_{C2} = \frac{D_1 V_{\text{Low}}}{(1 - D_1)(1 - N)}. \tag{25}$$

Finally, the voltage of the high voltage port and step-up voltage gain are calculated using (4):

$$V_{\text{High}} = V_{C2} + V_{C3} = \frac{D_1 + (1 - N)}{D_2(1 - N)} V_{\text{Low}} \longrightarrow M = \frac{V_{\text{High}}}{V_{\text{Low}}} = \frac{D_1 + (1 - N)}{D_2(1 - N)}. \tag{26}$$

Using the same method, the capacitors' voltage and step-down voltage gain can be calculated as follows:

$$\begin{cases} V_{C1} = \dfrac{1 - N}{(1 - D_2) + (1 - N)} V_{\text{High}}, \\[3mm] V_{C2} = \dfrac{1 - D_2}{(1 - D_2) + (1 - N)} V_{\text{High}}, \\[3mm] V_{C3} = \dfrac{(1 - N)(1 - D_2)}{(1 - D_2) + (1 - N)} V_{\text{High}}, \end{cases} \tag{27}$$

$$M_{\text{Buck}} = \frac{V_{\text{Low}}}{V_{\text{High}}} = \frac{D_2(1 - N)}{D_1 + (1 - N)}. \tag{28}$$

The peak voltage across power switch Q_3 (V_{Q3}) can be obtained from state 1 of step-up mode:

$$V_{Q3} = V_{C2} - V_{Lm}. \tag{29}$$

Replacing (3), (24), and (25) into (29), V_{Q3} is calculated as follows:

$$V_{Q3} = \frac{D_1}{D_2(1 - N)} V_{\text{Low}} - \frac{1}{1 - N}\left(\frac{D_1}{D_2} V_{\text{Low}} - \frac{1}{D_2} V_{\text{Low}}\right) = \frac{V_{\text{Low}}}{D_2(1 - N)}. \tag{30}$$
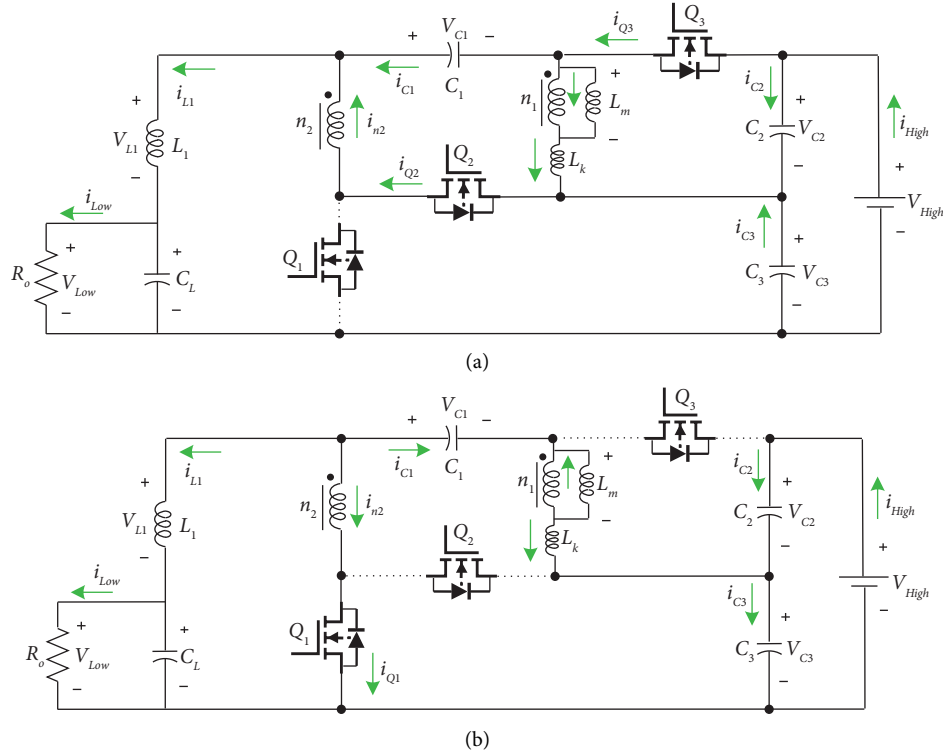
FIGURE 4: The equivalent circuits in step-down mode: (a) state 1 and (b) state 2.

Also, using step-up voltage gain, V_{Q3} can be expressed versus high voltage port:

$$V_{Q3} = \frac{V_{\text{High}}}{D_1 + (1 - N)}. \tag{31}$$

The peak voltage across power switch Q_2 (V_{Q2}) also can be achieved from state 1 of step-up mode:

$$V_{Q2} = V_{C1} + (1 - N)V_{Lm} = \frac{V_{\text{Low}}}{D_2}. \tag{32}$$

Finally, the peak voltage across power switch Q_1 (V_{Q2}) is calculated from state 2 of step-up mode:

$$V_{Q1} = V_{C3} = V_{Q2} = \frac{1 - N}{D_1 + (1 - N)}V_{\text{High}}. \tag{33}$$

Figures 5(a) and 5(b) show the voltage gain of the suggested structure in step-up and step-down operation modes versus duty cycle and turns ratio (N), respectively. A 3D view of the voltage gains is presented in Figure 6. Furthermore, Figure 7 illustrates the normalized peak voltage of the power switches versus N for $D_1 = 1 - D_2 = 1 - D_3 = 0.6$.

4.2. Currents Calculation.
The average current of the low voltage port (I_{Low}) is equal to the average current of inductor L_1 and is calculated versus the high voltage port current based on the voltage gain relation:

$$I_{\text{Low}} = MI_{\text{High}} = \frac{D_1 + (1 - N)}{D_2(1 - N)}I_{\text{High}}. \tag{34}$$

Considering the configuration of the proposed converter, the average current of power switches Q_2 and Q_3 is equal to the current of magnetizing inductance as follows:

$$I_{Q3} = I_{Q2} = I_{Lm} = I_{\text{High}}. \tag{35}$$

The average current of Q_1 can be written versus currents of low voltage port and power switch Q_2 as follows:

$$I_{Q1} = I_{\text{Low}} - I_{Q2} = (M - 1)I_{\text{High}} = \frac{D_1(2 - N)}{D_2(1 - N)}I_{\text{High}}. \tag{36}$$

Using the average currents obtained, the power switches current stresses are determined as follows:

$$\begin{cases} i_{Q1} = \dfrac{(2 - N)}{D_2(1 - N)}I_{\text{High}}, \\[4mm] i_{Q2} = i_{Q3} = \dfrac{2}{D_2}I_{\text{High}}. \end{cases} \tag{37}$$

Also, the root mean square (RMS) currents of the power switches are calculated as follows:

$$\begin{cases} I_{Q1}^{\text{RMS}} = \dfrac{\sqrt{D_1}(2 - N)}{D_2(1 - N)}I_{\text{High}}, \\[4mm] I_{Q2}^{\text{RMS}} = I_{Q3}^{\text{RMS}} = \dfrac{2}{\sqrt{D_2}}I_{\text{High}}. \end{cases} \tag{38}$$

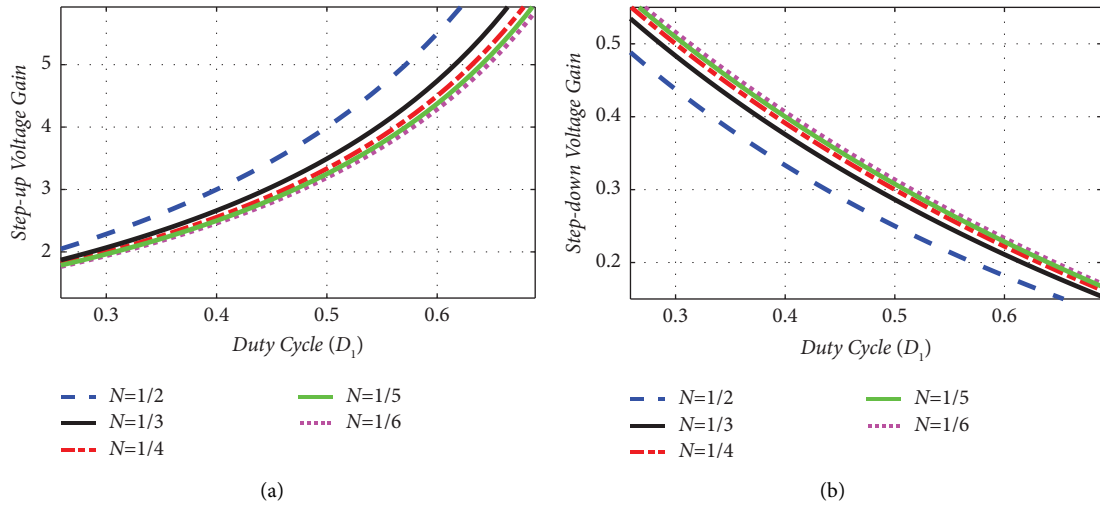Furthermore, the RMS currents of the coupled inductor and capacitors are summarized as follows:

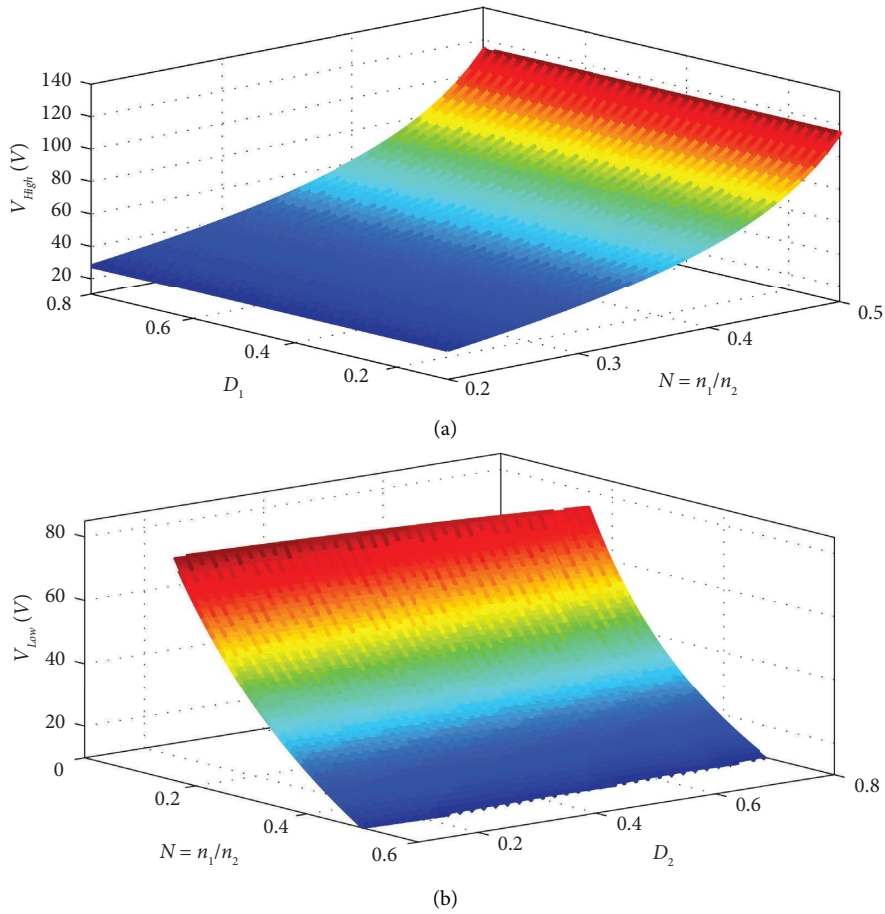FIGURE 5: Voltage gains versus duty cycle: (a) step-up and (b) step-down ($D_1 = 1 - D_2 = 1 - D_3$).

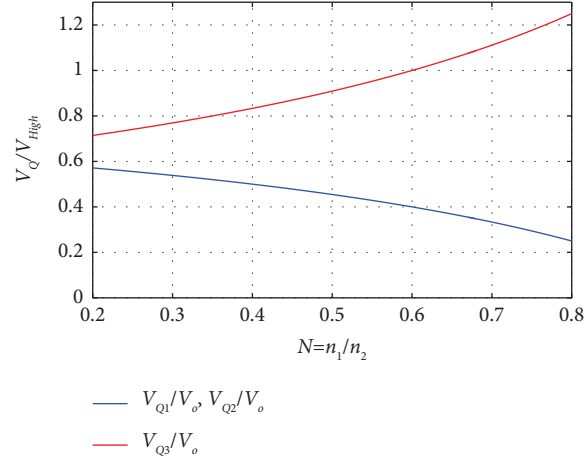FIGURE 6: 3D view of the voltage gains versus duty cycle: (a) step-up and (b) step-down.

FIGURE 7: Peak voltage versus duty cycle ($D_1 = 1 - D_2 = 1 - D_3 = 0.6$).

$$I_{n2}^{\text{RMS}} = \sqrt{\frac{D_1\left(2\left(1+D_1\right)-N\right)^2}{\left(D_2\left(1-N\right)\right)^2}+\frac{\left(D_1+\left(1-N\right)\left(1+D_1\right)\right)^2}{D_2\left(1-N\right)^2}}\,I_{\text{High}}, \tag{39}$$

$$\begin{cases} I_{C1}^{\text{RMS}} = \sqrt{\dfrac{D_1\left(1+D_1\right)^2+D_1^2\left(D_2\left(1-N\right)\right)^2}{\left(D_2\left(1-N\right)\right)^2}}\,I_{\text{High}}, \\[4mm] I_{C2}^{\text{RMS}} = \sqrt{\dfrac{1+D_2}{D_2}}\,I_{\text{High}}, \\[4mm] I_{C3}^{\text{RMS}} = \sqrt{1+\dfrac{\left(2-N\right)^2}{\left(D_2\left(1-N\right)\right)^2}}\left(D_1 I_{\text{High}}\right). \end{cases} \tag{40}$$

5. Design Considerations

This section presents the design process of each capacitor and inductor. For this work, the currents and voltages obtained in the previous section are used.

5.1. Inductors.
The minimum value of inductors L_1 and L_m is calculated based on the following equation:

$$L \geq \frac{DV_L}{20\% f_s I_L}. \tag{41}$$

For attaining CCM operation, the inductor current ripple is considered 20% of the average current. Therefore, the value of L_1 and L_m can be expressed as follows:

$$\begin{cases} L_1 \geq \dfrac{D_1 V_{L1}}{20\% f_s I_{L1}} = \dfrac{D_1 V_{\text{Low}}}{20\% f_s\left(1-N\right)I_{\text{Low}}}, \\[4mm] L_m \geq \dfrac{D_1 V_{Lm}}{20\% f_s I_{Lm}} = \dfrac{D_1{}^2 V_{\text{Low}}}{20\% f_s D_2\left(1-N\right)I_{\text{High}}}. \end{cases} \tag{42}$$

5.2. Capacitors.
The minimum value of capacitors C_1, C_2, and C_3 is calculated based on the following equation:

$$C \geq \frac{DI_C}{2\% f_s V_C}. \tag{43}$$

ΔV_C is defined as the voltage ripple of the capacitors and considered $\Delta V_C \leq 2\% V_C$. Thus, the minimum value of each capacitor can be obtained by the following equation:

$$\begin{cases} C_1 \geq \dfrac{D_1 I_{C1}}{2\% f_s V_{C1}} = \dfrac{D_1 I_{\text{High}}}{2\% f_s V_{\text{Low}}}, \\[4mm] C_2 \geq \dfrac{D_1\left(1-N\right)I_{\text{High}}}{2\% f_s V_{\text{Low}}}, \\[4mm] C_3 \geq \dfrac{D_1{}^2\left(2-N\right)\left(1-D\right)I_{\text{High}}}{2\% f_s D_2\left(1-N\right)V_{\text{Low}}}. \end{cases} \tag{44}$$

5.3. Coupled Inductor.
The magnetizing inductor is designed with an assumption as follows:

$$\Delta i_{L_m} \geq 20\% I_{L_m}. \tag{45}$$

On the other hand, the relationship between voltage and current of an inductor can be written as follows:

$$V_{L_m} = L_m \frac{d i_{L_m}}{dt}. \tag{46}$$

Therefore, the value of L_m can be obtained from (8) and (25) of the main manuscript file:

$$L_m \geq \frac{D_1 V_{\text{low}}}{20\% I_{Lm} f_s}. \tag{47}$$

The average current of L_m is calculated as follows:

$$I_{L_m} = I_o. \tag{48}$$

By replacing (48) with (47), the following equation can be obtained:

$$L_m \geq \frac{D_1 V_{\text{low}}}{20\% I_o f_s}. \tag{49}$$

The related equations for designing the size of the core, turn ratio, and the wire size are completely discussed in [33]. The coupled inductor is designed related to the maximum current of magnetizing inductances. Therefore, the magnetizing inductance should be defined, which is indicated in (47). The maximum current of magnetizing inductance current is equal to

$$I_{M,\max} = I_M + \Delta i_M. \tag{50}$$

The root mean square (RMS) of the winding current of the coupled inductor can be obtained as follows:

$$I_{\text{tot}} = i_{Lk1} + \frac{n_2}{n_1} i_{Lk2}. \tag{51}$$

In order to design the coupled inductor in detail, the following steps are utilized [30]:

(i) Determine core size $(k_g \geq (\rho L_M{}^2 I_{\text{tot}} I_{M.\max}{}^2 \times 10^8)/(B_{\max}{}^2 P_{cu} k_u))$

(ii) Determine the air gaps are neglected

(iii) Determine the winding number of the first side of the coupled inductor $(n_1 = (L_M I_{M,\max} \times 10^4)/(B_{\max} A_c))$

(iv) Determine the winding number of the second side of the coupled inductor $(n_2 = (n_1/2))$

(v) Evaluate the fraction of window area allocated for each winding $(a_1 = (n_1 I_1/I_{\text{tot}}), a_2 = (n_2 I_2/n_1 I_{\text{tot}}))$

(vi) Evaluate the wire size $(A_{w1} \leq (a_1 k_g W_A/n_1), A_{w2} \leq (a_2 k_g W_A/n_2))$

It has to be mentioned that in order to design the coupled inductor, the EPCOS B66344 (Ferrite core EE60) model is utilized. The magnetizing inductance (L_m) is chosen at $200\,\mu\text{H}$. For the coupled inductor with $L_m = 200\,\mu\text{H}$, the number of the first side of the coupled inductor winding is 34 turns, and also, the number of the second side of the coupled inductor winding is 68 turns. Regarding equation (52), if we consider the coupling coefficient about 0.98 and $L_m = 200\,\mu\text{H}$ in the experimental result, the leakage inductance (L_k) can be calculated as follows:

$$K = \frac{L_m}{L_m + L_k}. \tag{52}$$

By solving equation (52), the leakage inductance (L_k) is obtained about $4.08\,\mu\text{H}$. Extreme care has been taken in the design of the coupled inductor to have a low leakage inductance.

5.4. Power Switches.
The switching frequency of the proposed converter has been selected according to the available facilities in the laboratory, and the frequency of $50\,\text{kHz}$ is suitable for laboratory structures and is also large enough to reduce the size of the elements. For determining the volume and the cost of the components, the main factor is normalized voltage stress (NVS) throughout the semiconductors which is equal to (V_{PEAK}/V_o) and should be defined. In the recommended converter, only three semiconductor devices are utilized. The switches Q_1, Q_2, and Q_3 are the main semiconductor elements of the presented structure. The NVS throughout the switches is defined as follows:

$$\begin{cases} V_{Q1} = \dfrac{1-N}{D_1 + (1-N)} V_{\text{High}}, \\[2ex] V_{Q2} = \dfrac{V_{\text{Low}}}{D_2}, \\[2ex] V_{Q3} = \dfrac{V_{\text{High}}}{D_1 + (1-N)}. \end{cases} \tag{53}$$

The switch current stress is explained as follows:

$$\begin{cases} i_{Q1} = \dfrac{(2-N)}{D_2(1-N)} I_{\text{High}}, \\[2ex] i_{Q2} = i_{Q3} = \dfrac{2}{D_2} I_{\text{High}}. \end{cases} \tag{54}$$

Based on (53), it can be concluded that the maximum voltage throughout the switches is acceptable and low compared to the output voltage in the multi-input converters. Besides, the switches are selected based on the nominal value of voltage and current stress throughout the switches, which are indicated in (53) and (54).

6. Power Losses and Efficiency Analysis

In this section, the efficiency of the suggested bidirectional converter is analyzed. The efficiency is determined based on the following relation:

$$\eta = \frac{\text{Output Power}}{\text{Output Power} + \text{Total Losses}} \times 100\%, \tag{55}$$

where *Total Losses* of the proposed converter are defined as follows:

$$\text{Total Losses} = \Delta P_{\text{Switches}} + \Delta P_{\text{Capacitors}} + \Delta P_{\text{Inductors}}, \tag{56}$$

$\Delta P_{\text{Switches}}$ is the losses of the switches Q_1, Q_2, and Q_3 which is obtained as follows:

$$
\begin{aligned}
\Delta P_{\text{Switches}} &= \Delta P_{\text{Conduction}} + \Delta P_{\text{Switching}} \\
&= \sum_{i=1}^{3} r_{ds\_on_i} \left(I_{Qi}^{\text{RMS}}\right)^2 + \sum_{i=1}^{3} \frac{1}{2} f_s (T_{Ri} + T_{Fi}) I_{Qi} V_{Qi}.
\end{aligned}
\tag{57}
$$

In (57), r_{ds} is the ON-state resistance of switches. I_Q and V_Q refer to the average current and voltage across the switch Q. Average current of the switches has been calculated in subsection 4.2. T_R and T_F are the rise and fall times, respectively, available in the switches datasheet. The losses of capacitors and inductors are calculated based on RMS currents and equivalent series resistance (r_C and r_L) values as follows:

$$\Delta P_{\text{Capacitors}} = \sum_{i=1}^{3} r_{Ci} \left(I_{Ci}^{RMS}\right)^2,$$

$$\Delta P_{\text{Inductors}} = r_{L1} \left(I_{L1}^{RMS}\right)^2 + \left(\frac{r_{n1}}{N} + r_{n2}\right) \left(I_{n2}^{RMS}\right)^2. \tag{58}$$

7. Comparison Study

This part summarizes the comparison of the proposed topology and other similar topologies. In this comparison, input current ripple, peak voltage across semiconductors, step-up voltage gain, rated power, efficiency, switching frequency (f_s), bidirectional features, and the total number of used elements include power switches, power diodes, capacitors, and magnetic cores are taken into account.

Among the converters introduced in Table 1, the converters in [11, 14, 17, 19, 25], and [26] employ four power switches, and the converter in [27] includes five power switches. Additionally, all the structures in Table 1 contain a minimum of one power diode, while the power diode does not exist in the proposed topology. On the other hand, the proposed converter has only eight elements in its structures which are the minimum value among the converters in this table. The input current ripple is an essential parameter for renewable energy and HESs. According to Table 1, the converters in [14, 19, 25], and [27] suffer from high input current ripple and discontinued current. The comparison of the peak voltage across power switches shows that [14, 19, 25], and [27] have higher peak voltage than other topologies.

Also, the suggested topology has a lower peak voltage across power switches with comparable voltage gain than other converters. The converters in [11, 25–27] are built with higher-rated power. However, the efficiency is not reported in these papers. The proposed converter has higher efficiency at the same output power (80 W). Finally, the suggested bidirectional topology is built with a 50 kHz switching frequency higher than other converters. As a result,

considering the comparison of the proposed converter and different similar topologies, it can be mentioned that the suggested bidirectional DC-DC converter benefits from the low number of components, higher efficiency, lower peak voltage across power switches, justifiable voltage gain, and rated power. These advantages make the proposed topology proper for EVs and other applications such as renewable energy systems.

8. Controller Method

The proposed paper control design in both step-up and step-down modes is carried out in this section. If the duty cycle of the power switches is controlled properly, the voltage will be adjusted. In order to design the controller for the suggested converter, the dynamic analysis should be provided. The state-space average method is utilized for dynamic modeling. The system equations are prepared as the state, input, and control variable functions which are indicated in the state-space form in the following [32]:

$$
\begin{aligned}
\widehat{x}'_i(t) &= A\widehat{x}_i(t) + B\widehat{u}_i(t), \\
\widehat{y}_i(t) &= C\widehat{x}_i(t) + D\widehat{u}_i(t).
\end{aligned}
\tag{59}
$$

In (18), $\widehat{x}'_i(t)$ is the vector of state variables, $\widehat{u}_i(t)$ is the vector of input variables, and $\widehat{y}_i(t)$ is the vector of output variables which are expressed as follows for both boost and buck operation modes:

$$
\begin{aligned}
&\begin{cases}
\widehat{x} = \left[\widehat{i}_{L1}, \widehat{i}_{Lnl}, \widehat{i}_{Ln2}, \widehat{v}_{C1}, \widehat{v}_{C2}, \widehat{v}_{C3}\right]^T \\
\widehat{u} = \left[\widehat{v}_{\text{low}}, \widehat{i}_{\text{high}}, \widehat{d}_1, \widehat{d}_2\right]^T \qquad \longrightarrow \text{Step} - \text{up}, \\
\widehat{y} = \left[\widehat{i}_{\text{low}}, \widehat{v}_{\text{high}}\right]^T
\end{cases} \\
&\begin{cases}
\widehat{x} = \left[\widehat{i}_{L1}, \widehat{i}_{Lnl}, \widehat{i}_{Ln2}, \widehat{v}_{C1}, \widehat{v}_{C2}, \widehat{v}_{C3}\right]^T \\
\widehat{u} = \left[\widehat{v}_{\text{high}}, \widehat{i}_{\text{low}}, \widehat{d}_1, \widehat{d}_2\right]^T \qquad \longrightarrow \text{Step} - \text{down}. \\
\widehat{y} = \left[\widehat{i}_{\text{high}}, \widehat{v}_{\text{low}}\right]^T
\end{cases}
\end{aligned}
\tag{60}
$$

In dynamic modeling, the following assumptions are considered.

(i) All passive and active elements are considered ideal

(ii) The voltage ripple of the capacitors is ignored

Therefore, by considering the above considerations, the equations related to the state and output variables can be achieved by using Kirchhoff's voltage and current principles.

The dynamic performance of the recommended structure can be indicated with a small-signal frequency response. In this section, the values of the elements are presented in Table 2 and the "Experimental" result section. The simulation result of the control to the output transfer function in the Laplace domain (the magnitude dB and phase frequency response) for boost mode and buck mode has been demonstrated in Figures 8(a) and 8(b), respectively. The closed-loopsmall-signal transfer function from the output voltage to each duty cycle is illustrated in Figure 8(c). The output voltage can be controlled properly by using a proportional-

TABLE 1: Comparison of the proposed converter with other topologies.

Specification	[11]	[14]	[17]	[19]	[25]	[26]	[27]	Proposed
Total no. of elements	11	13	12	10	10	11	12	8
No. of capacitors	1	2	2	4	2	3	1	3
No. of magnetic cores	2	2	2	1	1	2	2	2
No. of diodes	4	5	4	1	3	2	2	0
No. of power switches	4	4	4	4	4	4	7	3
Input current ripple	Low	High	Low	High	High	Low	High	Low
Peak voltage across semiconductors	$V_{High} - V_{Low}$	V_{High}	$V_{High} - V_{Low}$	V_{High}	V_{High}	Not reported	V_{High}	$V_{High}/(D+1-N)$
Step-up voltage gain	$(1-D^2)/(1-(D+1)D)$	$(1-D_1)/(D_2(1-D_2-D_2)-D_1)$	$(D^2-D+1)/((1-D)^2)$	$1/(1-D)$	$1/(1-D)$	Not reported	Not reported	$(D-N+1)/((1-N)D)$
Bidirectional	√	√	√	√	√	√	√	√
Eff. at 80 W	Not reported	90%	90%	Not reported	Not reported	Not reported	Not reported	95.22%
Rated power (W)	220	80	140	85	236	200	200	120
f_s (kHz)	20	30	30	0.4	10	40	40	50

integral (PI) controller. The proper interpolation is produced by comparing the appropriate duty cycle with a carrier wave. It has to be mentioned that the PI controller includes a gain and time constant that the values of them are obtained by a trade-off. By defining a reference current and voltage for the expected power level of the proposed converter, the current of the inductor and output voltage are read. If there is a change in the values of the input ports, the command to regulate the voltage at the output and the inductor current is applied through the microcontroller, and it produces a suitable pulse for the power switches based on the load requirement.

9. Experimental Results

This section presents the experimental results of the proposed bidirectional converter, to verify the mathematical equations and the effectiveness of the suggested topology. The specifications of the experimental prototype are given in Table 2. The rated power in step-up mode operation is equal to 120 W, and the rated power in step-down operation is 50 W. The voltage conversion ratio in step-up mode is 20~110 V, and in step-down mode is 100~33 V. The results are presented in two subsections to demonstrate the step-up and step-down operations. The experimental prototype is added and is shown in Figure 9.

9.1. Step-Up Operation Mode. The power switches' gate PWM pulses are shown in Figures 10(a)–10(c). According to these figures, when Q_1 is turned on, Q_2 and Q_3 are turned off. The current waveform of L_1 is depicted in Figure 11(a). Its peak-to-peak and average values are 8.5 A and 7.5 A, respectively. The voltage across C_1, C_2, and C_3 is shown in Figures 11(b)–11(d), respectively. The voltage of C_1 is obtained at 29 V. Additionally, V_{C2} and V_{C3} are 57 V and 50 V, respectively. These results verify equations (23)–(25). The experimental voltage waveforms of the power switches are demonstrated in Figures 12(a)–12(c). The peak voltage across Q_1 is obtained at 50 V. Furthermore, based on Figures 12(a) and 12(b), the peak voltage over Q_2 and Q_3 is measured at 50 V and 97 V, respectively. The measured output voltage in step-up mode (V_{High}) is shown in Figure 12(d). As can be seen in this figure, V_{High} is obtained 108 V. Therefore, considering $V_{Low} = 20$ V, the experimental step-up voltage gain is equal to 5.4. This result verifies the presented theoretical step-up voltage gain in equation (26).

9.2. Step-Down Operation Mode. The power switches' gate PWM pulses in step-down operation mode are shown in Figures 13(a)–13(c). According to these figures, when Q_1 is turned off, Q_2 and Q_3 are turned on, simultaneously. The current waveform of L_1 is depicted in Figure 14(a). When Q_1 is turned on, i_{L1} is reduced, linearly. The average value of i_{L1} is measured at 1.7 A, which is obtained lower than the step-up mode. The voltage waveforms of capacitors C_1-C_3 are shown in Figures 14(b)–14(d). According to these figures, the voltage across C_1 is 22 V. Also, V_{C2} and V_{C3} are 44 V and 55 V, respectively, which verify the mathematical analysis of

TABLE 2: Experimental specifications.

Parameters	Step-up mode	Step-down mode
Input voltage	20 V	100 V
Output voltage	110 V	33 V
Output power (P_{out})	120 W	50 W
Frequency (f_s)	50 kHz	50 kHz
Duty cycle (D_1)	0.6	0.4
Duty cycle (D_2, D_3)	0.4	0.6
Components		
C_L	200 V/220 μF	
Q_1, Q_3, & Q_2	IRFP260N	
Capacitors C_1, C_2, and C_3	200 V/220 μF	
Inductors L_1	Ferric core (200 μH)	
Coupled inductor	Ferric core (200 μH, $N = 2/1$)	

step-down mode related to capacitors voltages (equation (27)). Additionally, based on Figures 11 and 14, in both step-up and step-down operation modes, the voltage ripple across used capacitors is significantly low. The power switch's voltage waveforms are demonstrated in Figures 15(a)–15(c). As can be seen in these figures, the voltages across power switches are obtained without spikes. Therefore, low-rated power switches can be used for the implementation of the proposed converter. The peak voltage across Q_1 is measured at 55 V. Furthermore, the peak voltage over Q_2 and Q_3 is achieved at 55 V and 110 V. The output voltage in step-down mode (V_{Low}) is depicted in Figure 15(d). Based on this figure, V_{Low} is measured at 33 V. Therefore, equation (28) can be verified by this experimental waveform. Considering $V_{High} = 100$ V, the experimental step-down voltage gain is equal to 0.33.

Measured power efficiency in step-up and step-down operation modes is depicted in Figure 16. In step-up mode, the lower efficiency is measured at 94.6% at 120 W, and maximum efficiency is obtained at 96.11% at 20 W. In step-down mode, the maximum efficiency is 94.43% at 50 W, and 92.79% is the lowest value. Based on the power losses analysis and the achieved result in the experimental section, the power losses calculation is presented in Table 3.

As described in previous sections, the suggested converter has a low-voltage port and a high-voltage port. This topology has the ability to operate in boost (discharging) and buck (charging) modes and share a bidirectional power flow between low-voltage and high-voltage ports. The main advantages of this converter are low component count, low volume, low cost, and high efficiency. The suggested converter can play an important role in supporting and recovering energy for the battery. In fact, this converter can transfer energy in two directions between two sources. The battery balances the transfer of energy between the load and the source. The voltage difference between the battery and the DC bus is high. Therefore, a bidirectional converter with high and low voltage conversion ratio is needed. Therefore, the recommended converter with mentioned features can be utilized as a supporting energy converter in EV with HESs applications. Considering the mathematical analysis and experimental results, the proposed converter has step-up

Bode Diagram
Gm = Inf, Pm = 90.1 deg (at 2e+04 rad/s)

(a)

Bode Diagram
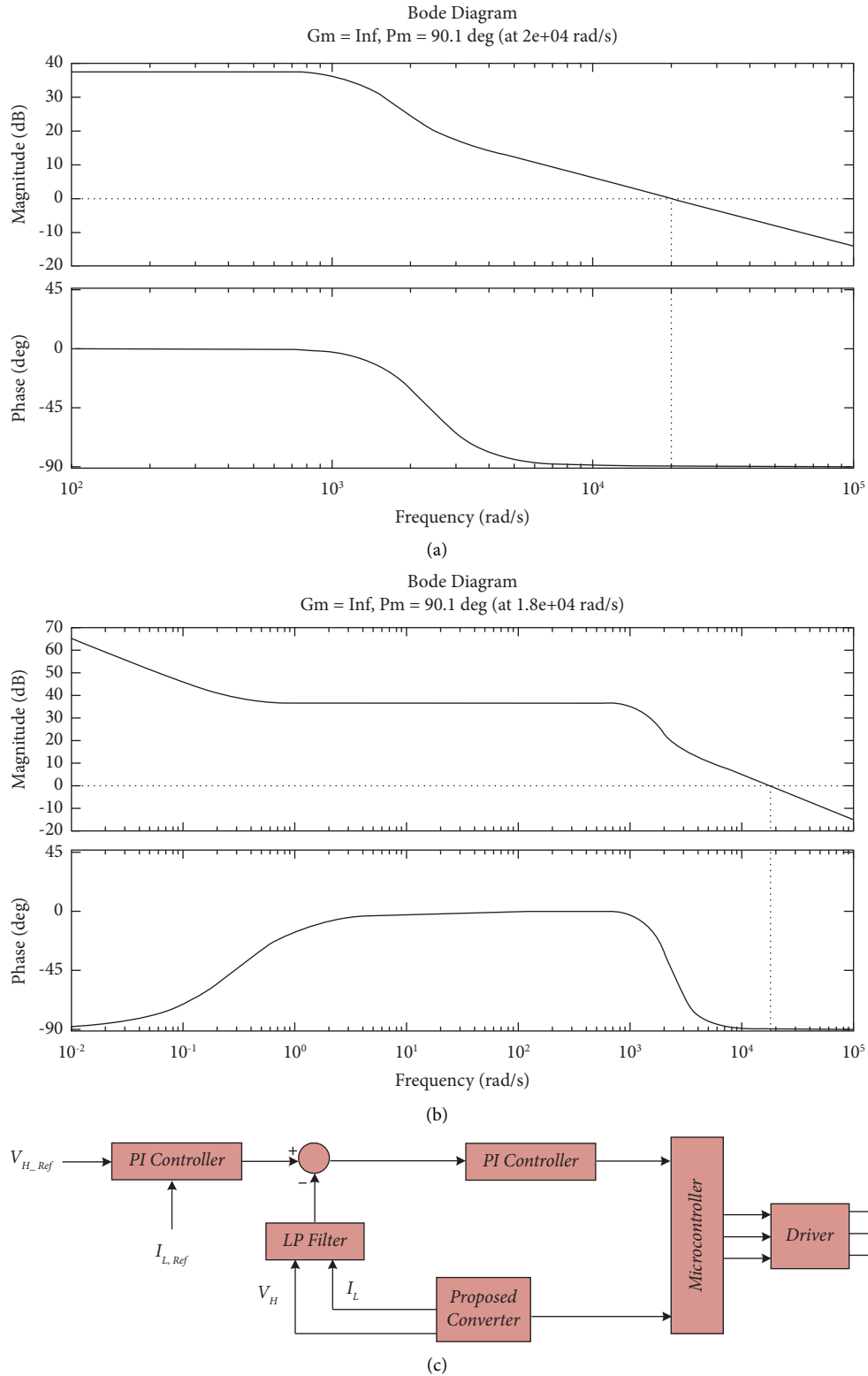Gm = Inf, Pm = 90.1 deg (at 1.8e+04 rad/s)

(b)

(c)

FIGURE 8: Bode plod and controller scheme of the suggested converter: (a) frequency response in boost mode, (b) frequency response in buck mode, and (c) control loop of the suggested structure.
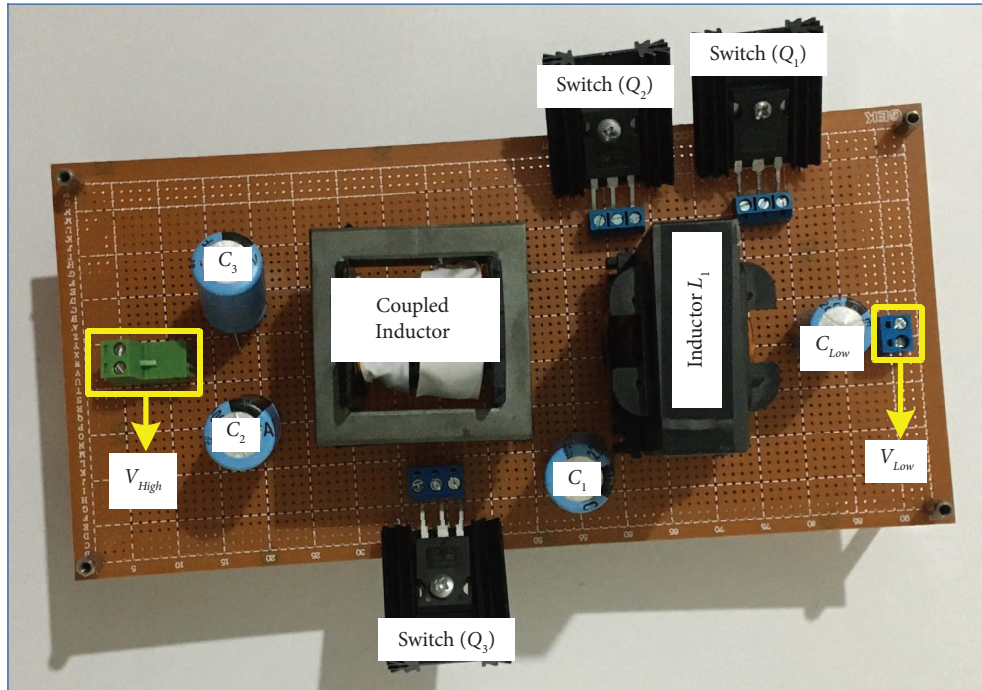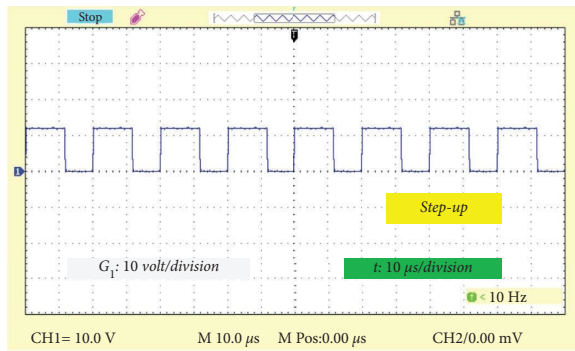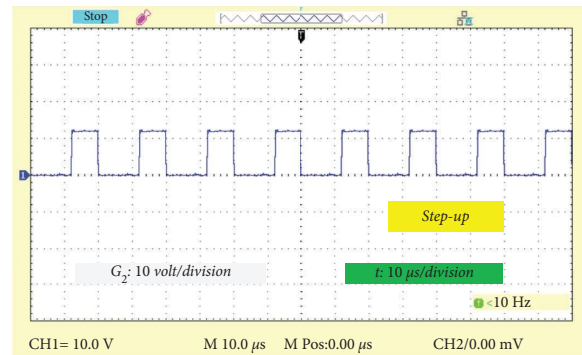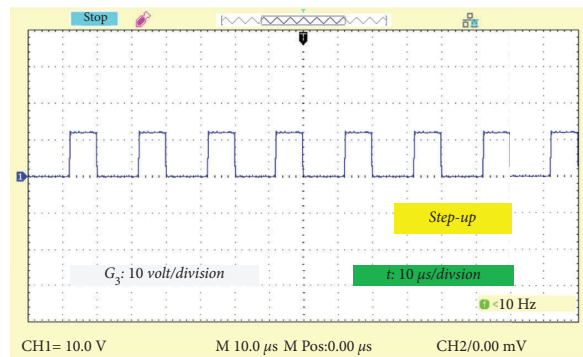
FIGURE 9: Experimental prototype of the suggested converter.

(a)

(b)

(c)

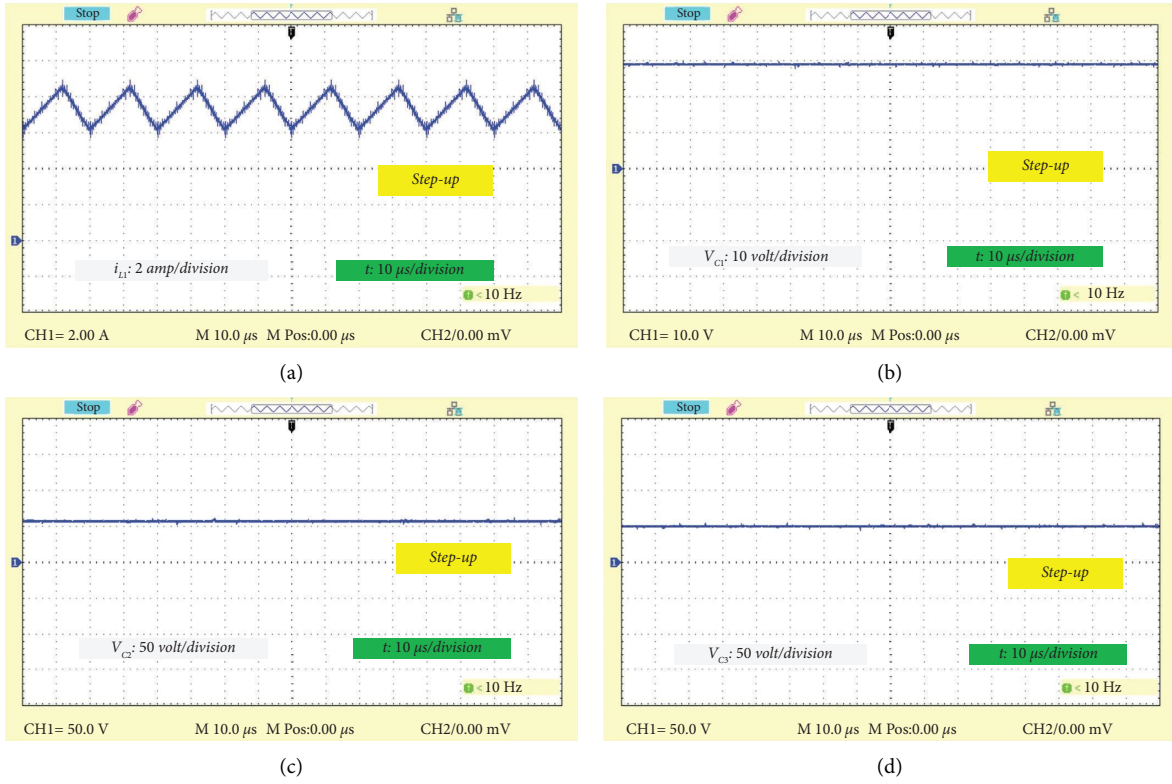FIGURE 10: Gate pulses in step-up operation mode: (a) V_{G1}, (b) V_{G2}, and (c) V_{G3}.

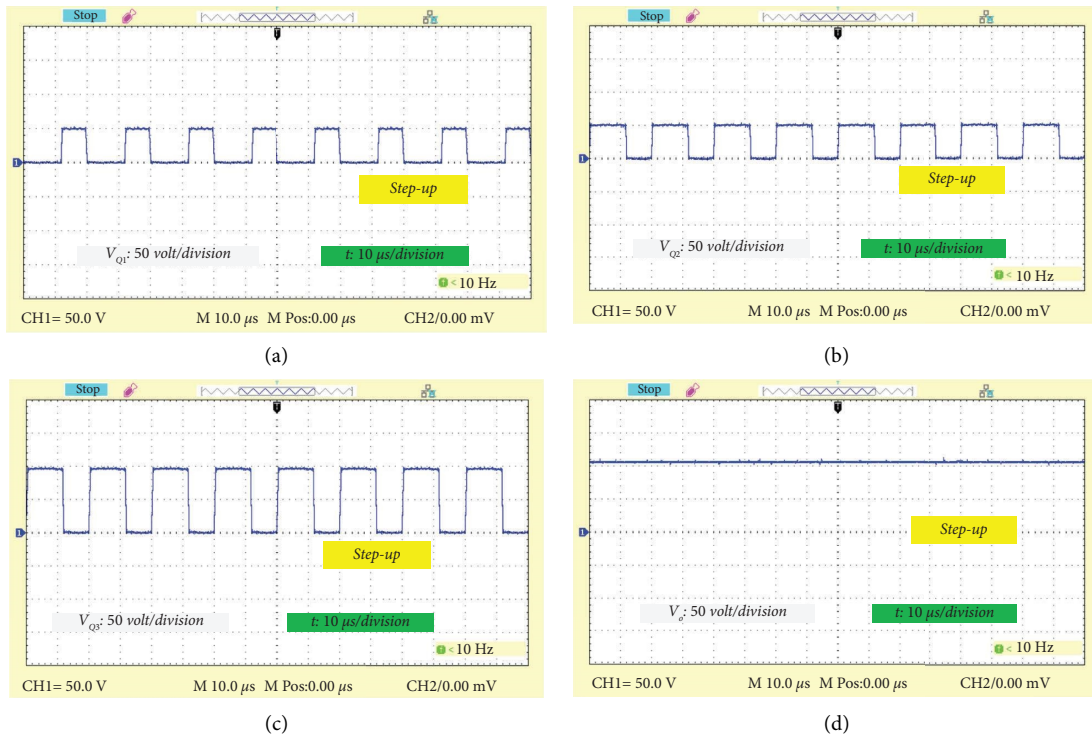FIGURE 11: Waveforms in step-up mode: (a) i_{L1}, (b) V_{C1}, (c) V_{C2}, and (d) V_{C3}.

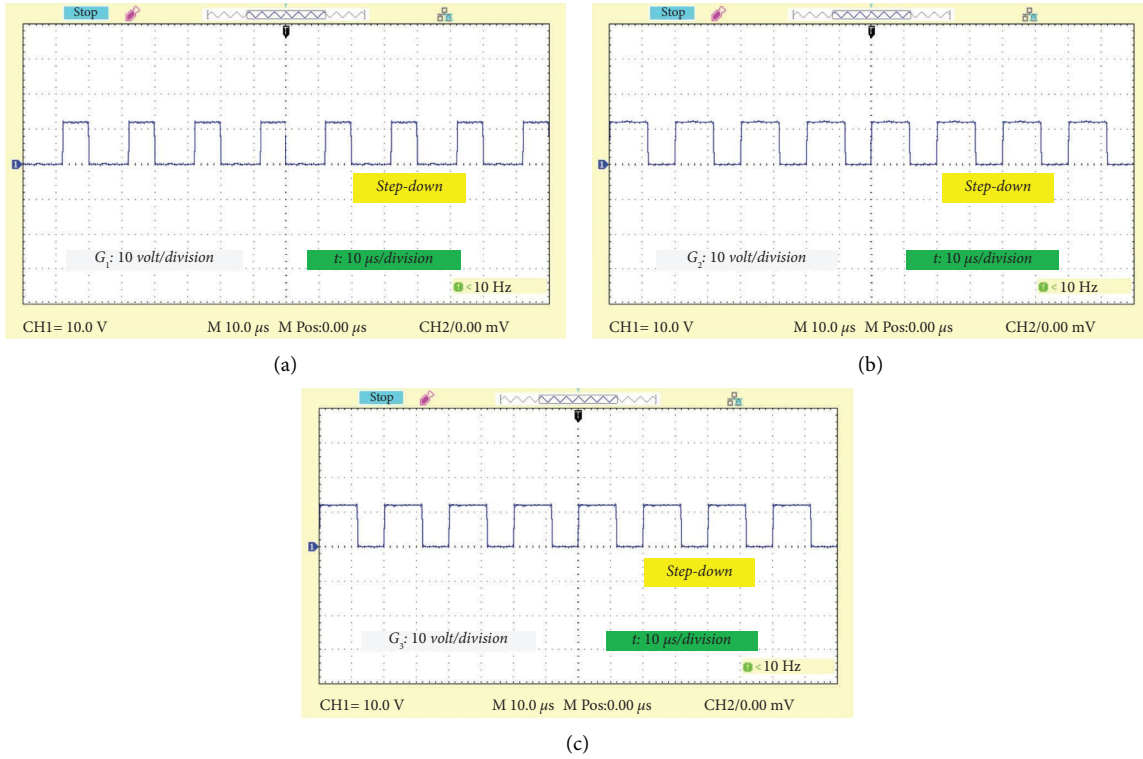FIGURE 12: Voltages in step-up operation: (a) V_{Q1}, (b) V_{Q2}, (c) V_{Q3}, and (d) V_o.

(a)

(b)

(c)

FIGURE 13: Gate pulse in step-down operation: (a) V_{G1}, (b) V_{G2}, and (c) V_{G3}.
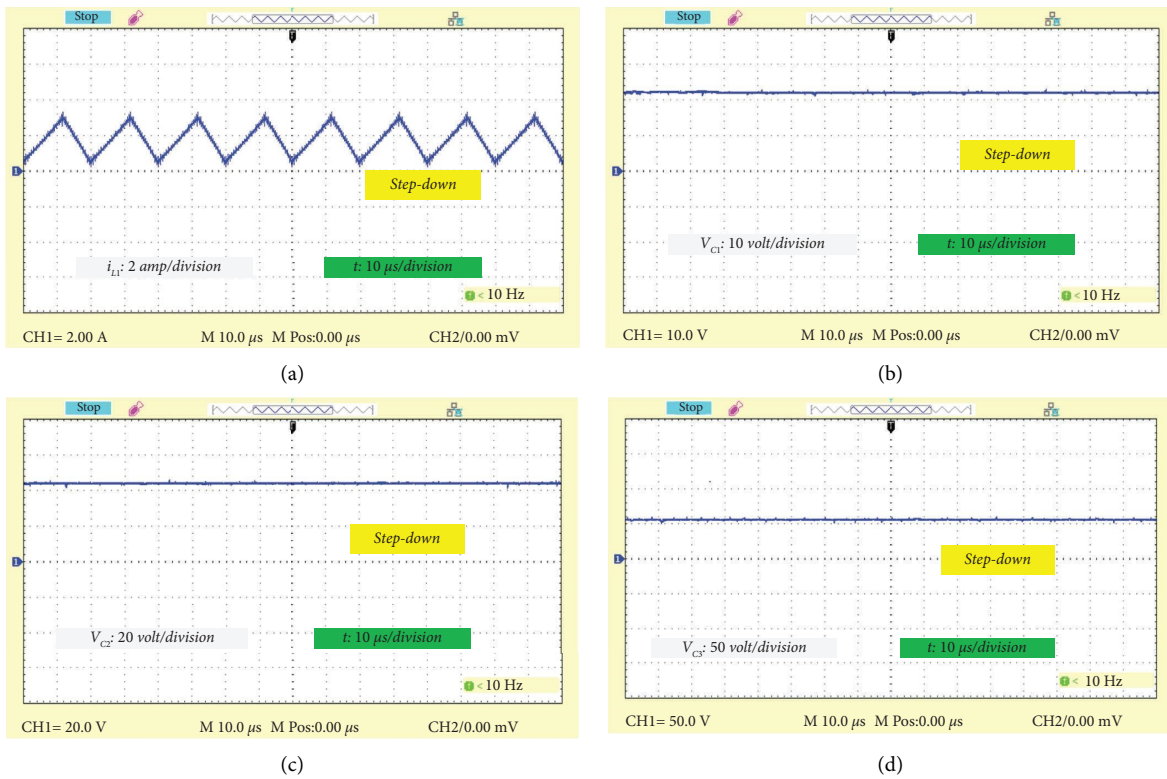

(a)

(b)

(c)

(d)

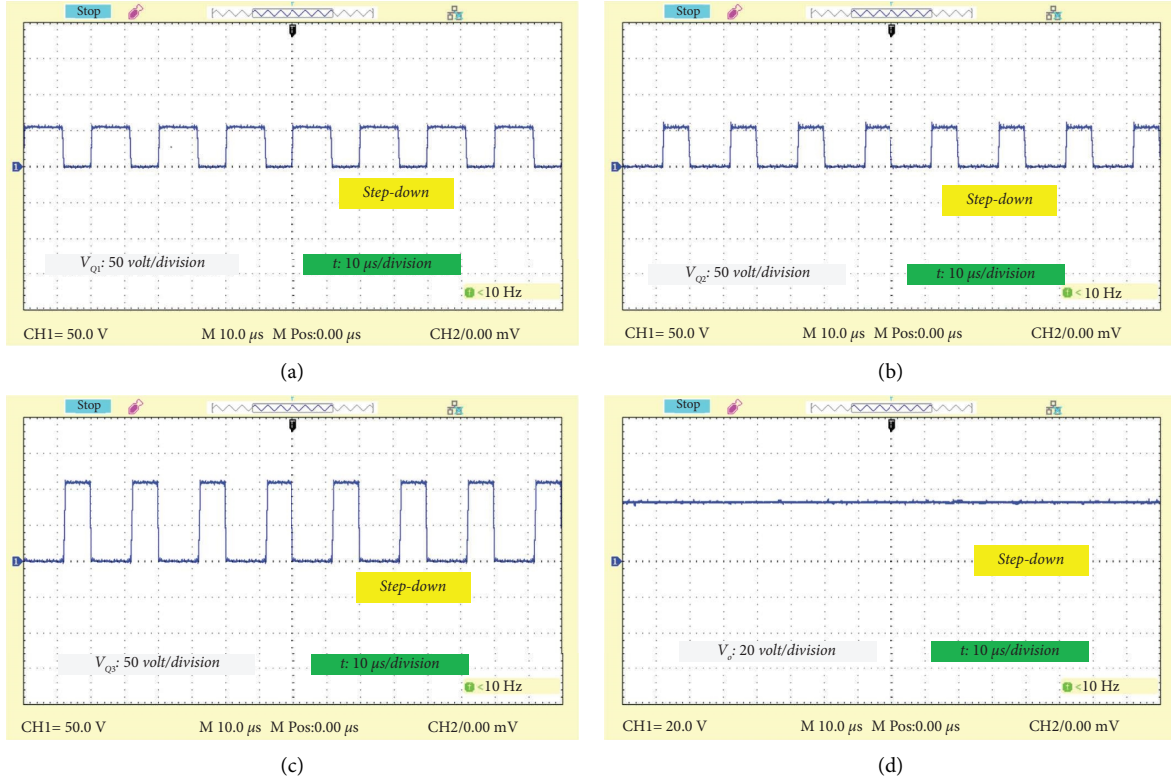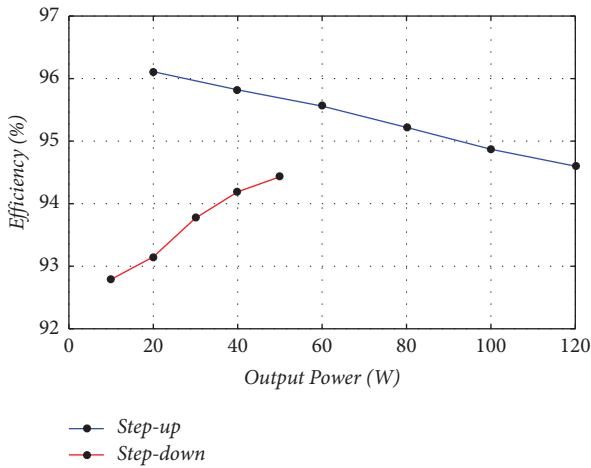FIGURE 14: Waveforms in step-down operation: (a) i_{L1}, (b) V_{C1}, (c) V_{C2}, and (d) V_{C3}.

FIGURE 15: Waveforms in step-down operation: (a) V_{Q1}, (b) V_{Q2}, (c) V_{Q3}, and (d) V_o.

FIGURE 16: Measured efficiency.

TABLE 3: Power loss specification in the step-up and step-down modes based on efficiency calculation.

Step-up mode	Step-down mode
$P_{\text{Switches}} = 3.48$ W	$P_{\text{Switches}} = 1.36$ W
$P_{\text{Inductors}} = 2.05$ W	$P_{\text{Inductors}} = 0.98$ W
$P_{\text{Capacitors}} = 1.31$ W	$P_{\text{Capacitors}} = 0.6$ W
Total losses = 6.84 W	Total losses = 2.94 W
Rated power = 120 W	Rated power = 50 W

and step-down operations, and bidirectional power flow is obtained. Additionally, high efficiency and low input current ripple make the presented converter sensible for EVs and renewable energy applications.

10. Conclusion

In this article, a high step-up, step-down DC-DC converter based on the coupled inductor technique for EV applications with bidirectional features was proposed. In this converter, a two-winding coupled inductor increases the voltage gain in both step-up and step-down operation modes. The current ripple of the low voltage port is low, which can be suitable for renewable energy sources like PV-based systems. Due to the low number of components, the power efficiency of the suggested topology is higher than similar topologies. Additionally, the proposed converter uses only three bidirectional semiconductors with low-rated voltages, which reduces the cost and volume. To demonstrate the performance of the proposed bidirectional DC-DC converter, operation modes, steady state, and efficiency analysis were presented. A comparison between the suggested converter and other similar converters was provided. Finally, the experimental results in step-up and step-down operations were presented. In step-up operation, the experimental prototype is tested for $f_s = 50$ kHz, $V_{\text{Low}} = 20$ V, $V_{\text{High}} = 110$ V, and rated power = 120 W, with 94.60%

efficiency. Furthermore, V_{High} is considered $100\,V$ with $V_{\text{Low}} = 33\,V$ and 94.43% efficiency at $50\,W$ rated power in step-down mode operation. Thus, with mentioned features, the proposed converter is sensible for EVs and renewable energy applications.

Data Availability

The raw data used for this proposed work have been cited in the manuscript. Moreover, the derived data supporting the findings of this study have been graphically depicted and are available with the corresponding author on request.

Conflicts of Interest

The authors declare that they have no conflicts of interest.

Acknowledgments

References

[1] M. Forouzesh, Y. P. Siwakoti, S. A. Gorji, F. Blaabjerg, and B. Lehman, "Step-up DC–DC converters: a comprehensive review of voltage-boosting techniques, topologies, and applications," *IEEE Transactions on Power Electronics*, vol. 32, no. 12, pp. 9143–9178, 2017.

[2] S. Pourjafar, F. Sedaghati, H. Shayeghi, and M. Maalandish, "High step-up DC–DC converter with coupled inductor suitable for renewable applications," *IET Power Electronics*, vol. 12, no. 1, pp. 92–101, 2019.

[3] T. Nouri, N. Vosoughi, S. H. Hosseini, E. Babaei, and M. Sabahi, "An interleaved high step-up converter with coupled inductor and built-in transformer voltage multiplier cell techniques," *IEEE Transactions on Industrial Electronics*, vol. 66, no. 3, pp. 1894–1905, 2019.

[4] S. M. Hashemzadeh, V. Marzang, S. Pourjafar, and S. Hossein Hosseini, "An ultra high step-updual-inputsingle-output DC-DC converter based on coupled inductor," *IEEE Transactions on Industrial Electronics*, vol. 69, no. 11, pp. 11023–11034, 2022.

[5] M. Z. Malik, H. M. H. Farh, A. M. Al-Shaalan, A. A. Al-Shamma'a, and H. H. Alhelou, "A novel single-input-multi-output converter for flexible-orderpower-distributive with MPPT capability," *IEEE Access*, vol. 9, pp. 131020–131032, 2021.

[6] H. Shayeghi, S. Pourjafar, S. M. Hashemzadeh, and F. Sedaghati, "Presenting of the magnetic coupling-basedtransformer-less high step-up DC-DC converter for renewable energy applications," *International Transactions on Electrical Energy Systems*, vol. 2022, Article ID 3141119, 15 pages, 2022.

[7] T. Liu, M. Lin, and J. Ai, "High step-up interleaved dc–dc converter with asymmetric voltage multiplier cell and coupled inductor," *IEEE Journal of Emerging and Selected Topics in Power Electronics*, vol. 8, no. 4, pp. 4209–4222, 2020.

[8] S. Pourjafar, H. Shayeghi, F. Sedaghat, and S. SeyedShenava, "A dual-input DC-DC structure with high voltage gain suggested for hybrid energy systems," *IET Power Electronics*, vol. 14, no. 10, pp. 1792–1805, 2021.

[9] H. Shayeghi, S. Pourjafar, and F. Sedaghati, "Presented a transformer-less buck-boost DC–DC structure with vast voltage range," *IET Power Electronics*, vol. 15, no. 7, pp. 659–674, 2022.

[10] S. Pourjafar, H. Shayeghi, S. M. Hashemzadeh, F. Sedaghati, and M. Maalandish, "A non-isolated high step-up DC–DC converter using magnetic coupling and voltage multiplier circuit," *IET Power Electronics*, vol. 14, no. 9, pp. 1637–1655, 2021.

[11] M. Z. Malik, H. Chen, M. S. Nazir et al., "A new efficient step-up boost converter with CLD cell for electric vehicle and new energy systems," *Energies*, vol. 13, no. 7, 2020.

[12] Y. Yuan-mao and K. W. E. Cheng, "Multi-inputvoltage-summation converter based on switched-capacitor," *IET Power Electronics*, vol. 6, no. 9, pp. 1909–1916, 2013.

[13] M. Ishigaki, K. Ishikawa, M. Kusakabe, and K. Tahara, "Multiport, bidirectional contactless connector for the interface of modular portable battery system," *IEEE Transactions on Power Electronics*, vol. 36, no. 2, pp. 1366–1375, 2021.

[14] R. R. Ahrabi, H. Ardi, M. Elmi, and A. Ajami, "A novel step-up multiinput DC–DC converter for hybrid electric vehicles application," *IEEE Transactions on Power Electronics*, vol. 32, no. 5, pp. 3549–3561, 2017.

[15] F. Akar, Y. Tavlasoglu, E. Ugur, B. Vural, and I. Aksoy, "A bidirectional nonisolated multi-input DC–DC converter for hybrid energy storage systems in electric vehicles," *IEEE Transactions on Vehicular Technology*, vol. 65, no. 10, pp. 7944–7955, 2016.

[16] M. Z. Malik, A. Farooq, A. Ali, and G. Chen, "A DC-DC boost converter with extended voltage gain," in *Proceedings of the MATEC Web of Conferences*, vol. 40, EDP Sciences, Hangzhou, China, January 2016.

[17] F. Kardan, R. Alizadeh, and M. R. Banaei, "A new three input DC/DC converter for hybrid PV/FC/battery applications," *IEEE Journal of Emerging and Selected Topics in Power Electronics*, vol. 5, no. 4, pp. 1771–1778, 2017.

[18] N. Swaminathan and Y. Cao, "An overview of high-conversionhigh-voltage DC–DC converters for electrified aviation power distribution system," *IEEE Transactions on Transportation Electrification*, vol. 6, no. 4, pp. 1740–1754, 2020.

[19] B. Wang, X. Zhang, and H. B. Gooi, "An SI-MISO boost converter with deadbeat-based control for electric vehicle applications," *IEEE Transactions on Vehicular Technology*, vol. 67, no. 10, pp. 9223–9232, 2018.

[20] G. Guru Kumar, K. Sundaramoorthy, S. Athikkal, and V. Karthikeyan, "Dual input superboost DC–DC converter for solar powered electric vehicle," *IET Power Electronics*, vol. 12, no. 9, pp. 2276–2284, 2019.

[21] Y.-F. Wang, L.-K. Xue, C.-S. Wang, P. Wang, and W. Li, "Interleaved high-conversion-ratio bidirectional DC–DC converter for distributed energy-storage systems—circuit generation, analysis, and design," *IEEE Transactions on Power Electronics*, vol. 31, no. 8, pp. 5547–5561, 2016.

[22] M. Z. Malik, Q. Xu, A. Farooq, and G. Chen, "A new modified quadratic boost converter with high voltage gain," *IEICE Electronics Express*, vol. 14, 2016.

[23] V. Karthikeyan and R. Gupta, "Multiple-input configuration of isolated bidirectional DC–DC converter for power flow control in combinational battery storage," *IEEE Transactions on Industrial Informatics*, vol. 14, no. 1, pp. 2–11, 2018.

[24] A. Samadian, S. M. Hashemzadeh, M. G. Marangalu, M. Maalandish, and S. H. Hosseini, "A new dual-input high

step-up DC–DC converter with reduced switches stress and low input current ripple," *IET Power Electronics*, vol. 14, no. 9, pp. 1669–1683, 2021.

[25] A. Nahavandi, M. T. Hagh, M. B. B. Sharifian, and S. Danyali, "A nonisolated multiinput multioutput DC–DC boost converter for electric vehicle applications," *IEEE Transactions on Power Electronics*, vol. 30, no. 4, pp. 1818–1835, 2015.

[26] T. Jalilzadeh, N. Rostami, E. Babaei, and S. H. Hosseini, "Bidirectional multi-port dc–dc converter with low voltage stress on switches and diodes," *IET Power Electronics*, vol. 13, no. 8, pp. 1593–1604, June 2020.

[27] T. Jalilzadeh, N. Rostami, E. Babaei, and S. H. Hosseini, "Design, analysis and implementation of a new three-port DC-DC converter with bidirectional capability," *IET Power Electronics*, vol. 14, no. 15, pp. 2490–2506, 2021.

[28] M. Rezvanyvardom, A. Mirzaei, M. Shabani et al., "Interleaved step-upsoft-switching DC–DC Boost converter without auxiliary switches," *Energy Reports*, vol. 8, pp. 6499–6511, 2022.

[29] H. Khalid, S. Mekhilef, M. B. Mubin et al., "Analysis and design of series-LC-switch capacitor multistage high gain DC-DC boost converter for electric vehicle applications," *Sustainability*, vol. 14, no. 8, p. 4495, 2022.

[30] B. Babes, S. Mekhilef, A. Boutaghane, and L. Rahmani, "Fuzzy approximation-basedfractional-order nonsingular terminal sliding mode controller for DC–DC buck converters," *IEEE Transactions on Power Electronics*, vol. 37, no. 3, pp. 2749–2760, 2022.

[31] M. Z. Malik, A. Ali, and D. Kumar, "A two cascaded boost converter with high voltage gain module," *International Journal of Computer and Electrical Engineering*, vol. 9, no. 2, pp. 476–483, 2017.

[32] T. Suntio, T. Messo, and J. Puukko, *Power Electronic Converters: Dynamics and Control in Conventional and Renewable Energy Applications"*, John Wiley & Sons, Hoboken, NJ, USA, 2017.

[33] R. W. Erickson and D. Maksimovic, *Fundamentals of Power Electronics*, Springer Science & Business Media, Berlin, Germany, 2007.